Relativistic Electron-Beam Transport Studies Using High-Resolution, Coherent Transition Radiation Imaging

Laser-generated relativistic electron beams have applications in compact, high-brightness laser–plasma particle accelerators,[1] narrowband x-ray sources for medical applications,[2] x-ray sources for ignition-scale, high-density inertial confinement fusion (ICF) target backlighter radiography,[3] collimated electron beams for free-electron lasers,[4] and collimated electron beams for the fast-ignition approach to ICF.[5] The fast electrons are generated by focusing short-pulse, high-intensity, $I \sim 10^{19}$ W/cm^2 laser light onto the front surface of planar-foil targets.[6] An understanding of the fast-electron generation and subsequent transport is essential for these applications.

The properties of fast electrons generated in short-pulse, high-intensity laser–solid interactions are studied using spatially resolved coherent transition radiation (CTR) emitted from the rear surface of planar targets.[7] Experiments employing CTR imaging with the highest spatial resolution reported, ~1.4 μm, are described.[8] The images contain bright, small-scale structures suggestive of electron-beam filamentation.[9] The small-scale features are embedded in larger annular-like structures. Analysis of the images suggests a fast-electron temperature of ~1.4 MeV and a half-angle divergence of ~16°. Three-dimensional (3-D) simulations of the fast-electron transport in planar, solid-density targets, using the hybrid-particle-in-cell (PIC) code *LSP*,[10] reproduce the details of the CTR images for an initial half-angle divergence of ~56°. The initial divergence is reduced in the target by a self-generated resistive magnetic field.[11]

CTR is emitted when an electron beam, with longitudinal electron-density modulations, crosses a refractive-index boundary, such as the rear surface of a target.[12] The density modulations drive a radiating, time-dependent polarization with strong frequency components at the modulation periodicity. The radiated energy is proportional to the square of the modulation amplitude and is strongly peaked in narrow spectral bands centered on the modulation frequencies.[7] Electron acceleration mechanisms that are active in high-intensity laser–solid interactions generate fast-electron beams with the required modulations. Acceleration by the laser electric field[6] drives electrons into the target once per optical cycle, whereas acceleration by the $v \times B$ component of the Lorentz force[6] drives electrons into the target twice per optical cycle. These electrons propagate through the target as a train of bunches separated in space by λ and $\lambda/2$, respectively, where λ is the laser wavelength. The density modulations are smeared out by refluxing,[13] so the CTR signal is produced by the electron's first pass through the target.

The experiments were conducted at LLE's Multi-Terawatt (MTW) Laser Facility.[14] A single laser pulse of wavelength $\lambda_L = 1053$ nm, with an energy of $E_L \sim 5$ J and a duration of $\Delta t_L \sim 500$ fs, was focused at normal incidence to a 4-μm-radius spot, producing an intensity of $I \sim 10^{19}$ W/cm^2. The laser pulse's intensity contrast ratio was ~10^3 at 1 ps before the peak of the pulse and ~10^8 at 50 ps before the peak. The Al, Cu, Sn, and Au foil targets had transverse dimensions of 500 μm and thicknesses ranging from 5 to 100 μm. A CTR diagnostic was fielded to acquire images of the rear-side optical emission with a spatial resolution of $\Delta \sim 1.4$ μm (Ref. 8). The images were captured on a scientific-grade charge-coupled-device (CCD) camera with a dynamic range of 10^4.

Figure 118.12 shows three characteristic images of the rear-surface emission plotted in arbitrary units of intensity on both a linear (top row) and logarithmic scale (bottom row). From left to right the targets are 20-μm-thick Al, 30-μm-thick Al, and 50-μm-thick Cu. The emission contains small-scale structures, with a mean diameter of ~4.0 μm, superimposed on a larger annular feature whose diameter increases with target thickness. The images are produced by light emitted at the target's rear surface with a wavelength $\lambda \sim 527$ nm, corresponding to the second harmonic of the incident laser. Imaging of the rear surface in an adjacent spectral window, centered on $\lambda =$ 480 nm, produced no measurable signal. The signal strength at $\lambda \sim 527$ nm implies that the emission is produced by a coherently driven mechanism—the most likely candidate being CTR from a density-modulated, relativistic electron beam, accelerated by the $v \times B$ component of the Lorentz force. The spatial distribution of the CTR emission suggests the electron-beam filaments.[9] The larger annular patterns suggest electron-beam hollowing and annular propagation.[15]

Figure 118.13(a) shows the spatially integrated CTR energy from 60 laser shots using Al, Cu, Sn, and Au foils of various thicknesses. Each point represents the mean CTR energy for the number of shots (two to five) taken at that thickness; the error bars are standard deviations and arise from shot-to-shot fluctuations. The integrated CTR energy decreases as the target thickness increases: for Al the decrease is about three orders of magnitude from 6 to 60 μm; for Au the decrease is about four orders of

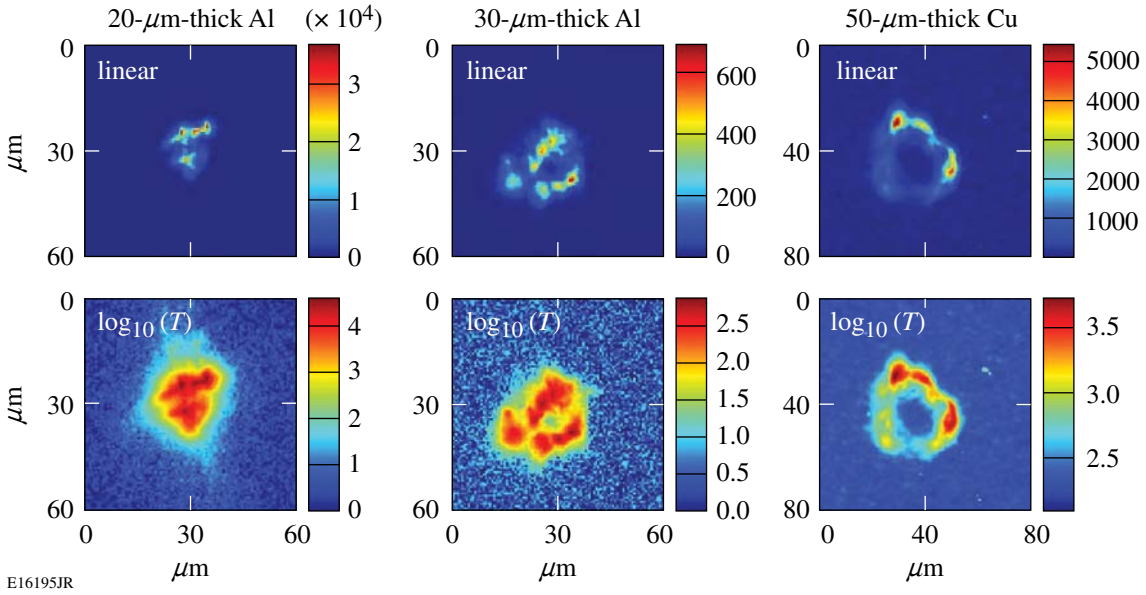

Figure 118.12
Images of the rear-surface optical emission, in arbitrary units of intensity, from thin foil targets illuminated at normal incidence with an intensity of $I \sim 10^{19}$ W/cm^2. The top row shows the emission on a linear scale while the bottom row uses a logarithmic scale. From right to left, the targets are 20-μm-thick Al, 30-μm-thick Al, and 50-μm-thick Cu. The images indicate the presence of bright small-scale structures that are embedded into a larger ringlike structure whose diameter increases with target thickness.

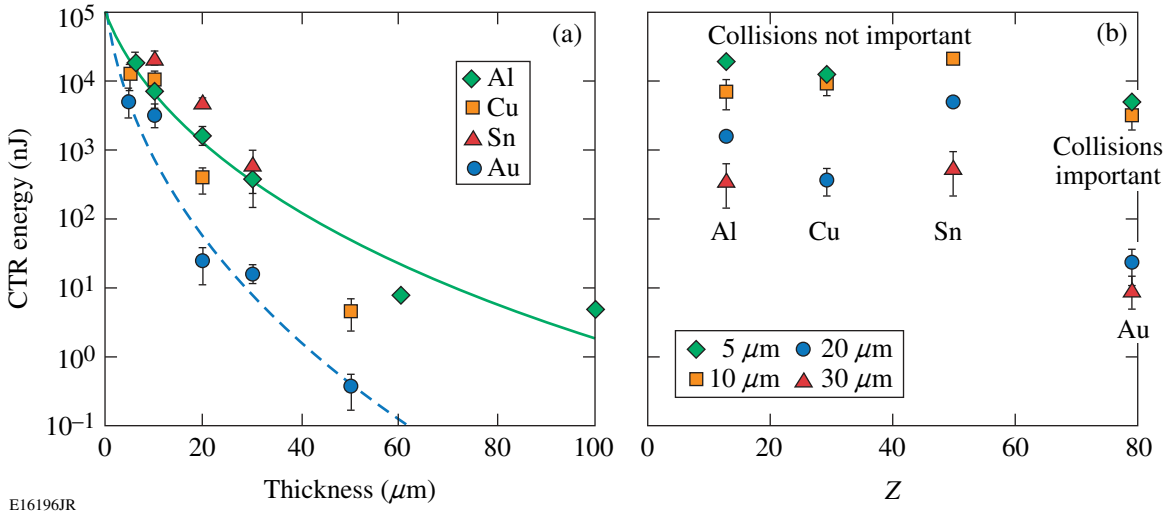

Figure 118.13
(a) The CTR signal decreases with increasing target thickness. The solid line is fitted to the Al data using the velocity dispersion model and is consistent with a fast-electron temperature of $T_{hot} \sim 1.4$ MeV. The dashed line is fitted to the Au data and is consistent with $T_{hot} \sim 0.9$ MeV. (b) The CTR energy's dependence on Z is weak for low- to mid-Z materials but significant for high-Z materials.

magnitude from 5 to 50 μm. The CTR energy's dependence on Z, at four different thicknesses, is shown in Fig. 118.13(b). Except for the highest-Z materials such as Au ($Z = 79$), the CTR energy does not depend on Z. For all thicknesses, the CTR signal is approximately constant from Al ($Z = 13$) to Sn ($Z = 50$). For the 5-μm targets, the CTR signal decreases by a factor of ~5 from Sn to Au, while for the 30-μm foils, the decrease from Sn to Au is approximately two orders of magnitude.

The CTR energy becomes dependent on target thickness because of fast-electron velocity dispersion. The velocity dispersion reduces the correlation between propagating bunches of electrons. This effect on the CTR signal has been quantified by Zheng *et al.*[12] The velocity dispersion model is used to estimate the fast-electron temperature T_{hot} from the variation of the CTR energy with target thickness. The solid line in Fig. 118.13(a) is fitted to the Al data; the variation in the CTR signal with increasing thickness is consistent with $T_{hot} = 1.4 \pm 0.1$ MeV. The dashed line shows that the corresponding fit to the Au data is consistent with $T_{hot} = 0.9 \pm 0.1$ MeV. The difference is attributed to collisional processes that also reduce the correlation between propagating electrons. The effect of fast-electron scattering from target atoms on the CTR signal has been estimated using the Monte Carlo code Geant4 (Ref. 16). A bunch of 1-MeV electrons were propagated along an electron-beam filament through 50 μm of Al or Au. The relative number of electrons remaining in the filament, as a function of distance, was used to estimate the variation in the CTR signal. The decrease in the CTR signal caused by scattering was found to be insignificant in Al. In Au, scattering's effect on the CTR signal became important after ~20 μm. This is seen in Fig. 118.13(b), where the measured CTR energy falls abruptly in Au targets for thicknesses ≥20 μm. Since it is not complicated by collisional effects, the result obtained from Al is taken to be the correct value for T_{hot}.

Figure 118.14 shows how the size of the rear-surface emission region grows with target thickness in the range from 5 to 100 μm; the values were determined by measuring the horizontal and vertical dimensions of the emission pattern. No dependence on the target material was observed, and each point represents the radial size averaged over all materials at each thickness. The half-angle electron-beam divergence was inferred to be $\theta_{1/2} \sim 16°$ using a least-squares linear fit. The linear fit intercepts the radial axis at ~4 μm, consistent with the laser focal spot being the source of the electron beam.

Due to the large range of spatial and temporal scales involved, the acceleration of electrons in high-intensity laser–solid interactions and their subsequent transport cannot be modeled simultaneously. The acceleration of electrons is modeled for short durations and small spatial scales using PIC codes with high temporal and spatial resolution.[17] Hybrid-PIC codes model the collisional transport of electrons over experimentally realistic spatial and temporal scales with restricted spatial and temporal resolution.[10] The details of the acceleration depend on the target's front-surface pre-plasma.[6,17] Behind the critical surface, the fast-electron beam is subject to the Weibel instability saturated by collisions as the electrons enter denser plasma.[17,18] State-of-the-art, 2-D PIC simulations resolve plasma densities up to 100× critical, while the electron density in the front of the target can be 10× higher.[17,18] Such simulations provide a large uncertainty in the initial angular divergence of electrons entering the target.

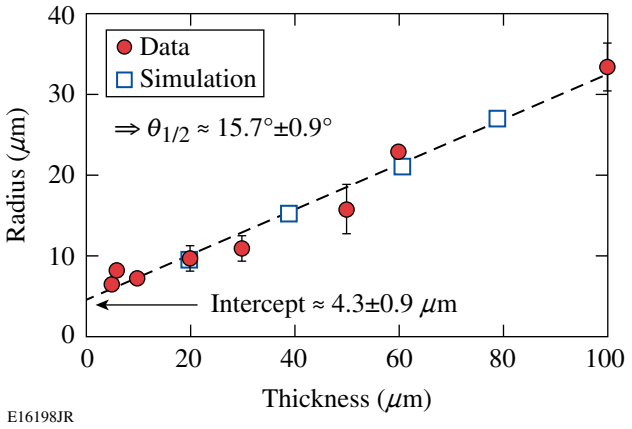

Figure 118.14
The transverse size of the rear-surface emission grows with target thickness. The dashed line shows a least squares fit to the experimental points and indicates a half-angle divergence of $\theta_{1/2} \sim 15.7° \pm 0.9°$. Numerical simulations of the electron transport reproduce the observed expansion.

The hybrid-PIC code *LSP*[10] modeled the 3-D transport of fast electrons in solid-density targets. In the target, fast electrons are collimated by a self-generated resistive magnetic field[19] and their angular divergence is reduced. The initial half-angle divergence was adjusted until the half-angle divergence in the target matched that observed in the experiments. This approach is different than that reported in Ref. 20, where the fast-electron acceleration was simulated but the electron transport in the target was not. The collimating effect of the resistive magnetic field in the target cannot be neglected. This approach predicts the initial fast-electron angular divergence, a quantity otherwise unavailable in absence of detailed 3-D PIC simulations. The *LSP* simulations predict a transverse fast-electron-density distribution that closely resembles the transverse distribution of CTR seen in the experiments.

In the simulations presented here, the fast electrons are injected (promoted from the background) with an exponential distribution, $\sim \exp\left(-E/\langle E_h \rangle\right)$, with a mean energy $\langle E_h \rangle$ given by the maximum of the ponderomotive[6] and Beg[21] scaling. The laser pulse was Gaussian in space and time with a duration of $\tau = 650$ fs, full width at half maximum (FWHM), a focal-spot size of 5.5 μm (FWHM), and a maximum intensity of $I = 1.45 \times 10^{19}$ W/cm^2, consistent with the parameters of the MTW laser. The laser-to-fast-electron energy conversion efficiency was 20% and independent of the laser intensity.[22] The initial electron-beam half-angle divergence is given by $\theta_{1/2} = \alpha \tan^{-1}\left[\sqrt{2/(\gamma-1)}\right]$, where $\gamma = \left(1 - v^2/c^2\right)^{-1/2}$, v is the fast-electron velocity, and c is the speed of light. Electrons with energy $E = (\gamma - 1)mc^2$, where m is the electron mass, are randomly injected in a cone of half-angle $\theta_{1/2}$, which for $\alpha = 1$ describes the angle at which electrons are ejected from a focused laser by the ponderomotive force.[23] Simulations were performed for 6×-, 8×-, and 10×-ionized Al targets with transverse dimensions of 120 μm and thicknesses of 20, 40, 60, and 80 μm. The plasma's Spitzer resistivity was saturated at low temperature according to $\eta = 1/\sqrt{\eta_{max}^{-2} + \eta_{sp}^{-2}}$, where $\eta_{max} = 1.6 \times 10^{-6}$ Ωm (Ref. 24) and $\eta_{sp} \propto Z/T^{3/2}$, where Z is the atomic number and T is the background temperature.[25] A broad vacuum region surrounded the target and the simulations used conducting boundaries. The spatial resolution was 1 μm in the longitudinal (z) and transversal (x and y) directions for $|x|, |y| < 30$ μm, with the transverse resolution gradually increased to 3 μm for $|x|, |y| > 30$ μm.

Simulations performed for $\alpha = 1$ in 8× ionized Al showed the half-angle divergence in the target to be $\theta_{1/2} \sim 16°$, as observed in the experiments. This result could be reproduced in the 6×- and 10×-ionized Al by varying α by 7%. Figure 118.15 shows the density distribution of fast electrons, with energy >250 keV, at the back of the target for $\alpha = 1$ and different target thicknesses. The density distributions are averaged in time using $\int n(\mathbf{r},t)dt/1.65\,\tau$, where $\mathbf{r}$ is the radial coordinate of the density. Although the distribution of CTR is not calculated, the spatial distribution of the fast-electron density at the rear surface, predicted by *LSP*, reproduces the details of the CTR emission pattern. The spot size in the simulations is also plotted as a function of the target thickness in Fig. 118.14.

The reduction in the half-angle divergence of the beam is caused by a collimating, azimuthal, self-generated resistive magnetic field. The field is generated at the transverse edge of the electron beam and is most intense in the first 20 μm, close to the front surface. Figure 118.16(a) shows cross sections through the azimuthal magnetic field for the 60-μm target, 350 fs after the peak of the laser pulse. The magnetic field partially collimates the beam. A beam with initial half-angle divergence of $\theta_{1/2} = 56°$ (mean angle = 37°), averaged inside the FWHM of the beam's spatial and temporal distribution, is reduced to a beam with an angular distribution peaked at 16°. The variation of the electron-density distribution with target thickness resembles an expanding annulus that breaks, along its circumference, into filaments generated by the resistive filamentation instability. Figure 118.16(b) shows the location of the fast-electron-density isosurface (solid surface) at 50% of the peak density in the 60-μm target, 350 fs after the peak of the laser pulse; the semitransparent surface corresponds to

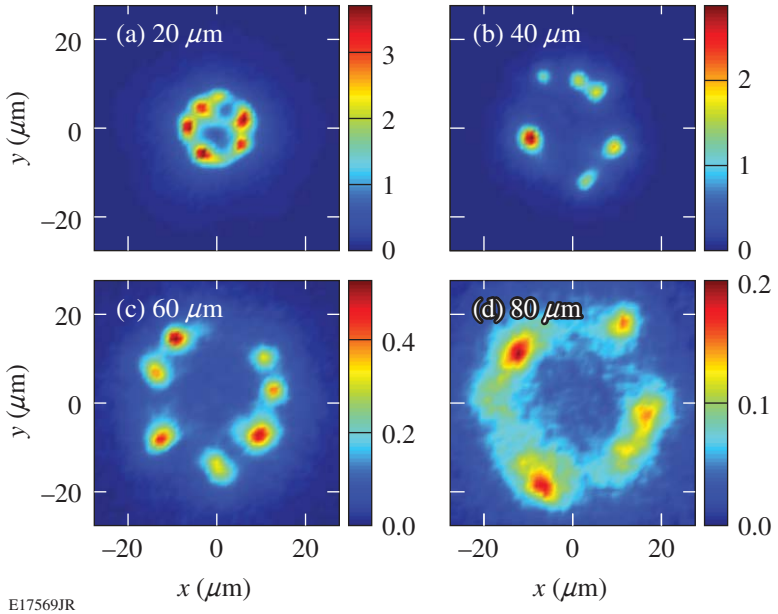

Figure 118.15
Predictions of the rear-surface, transverse density distribution of fast electrons for different thicknesses of Al (in units of 10^{20} cm^{-3}). The distributions closely resemble the measured rear-surface CTR distributions. The thickness for each target is specified on the figure.

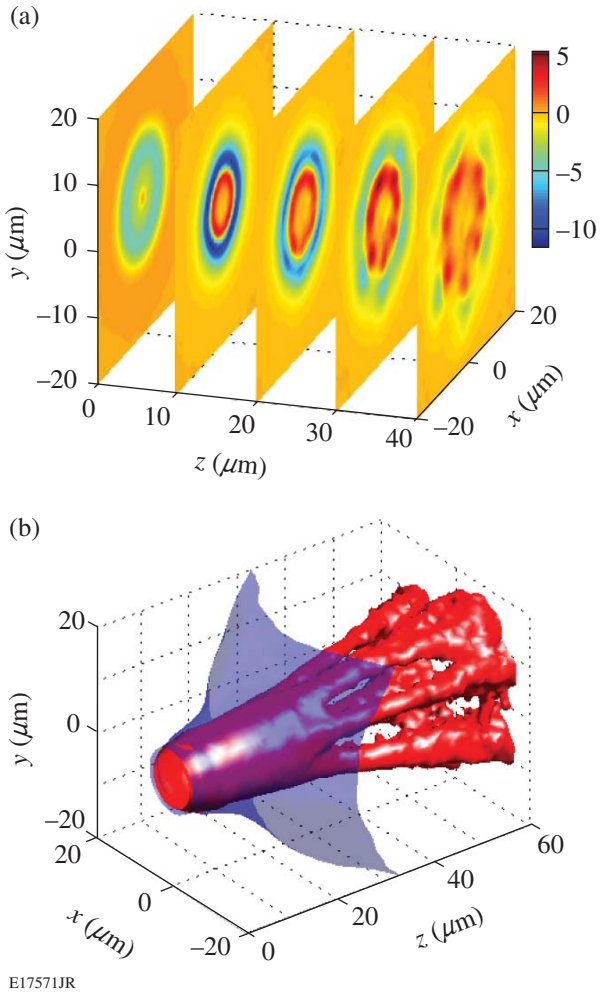

Figure 118.16
(a) Cross sections through the azimuthal magnetic field (in units of megaGauss) for the 60-μm target, 350 fs after the peak of the laser pulse. (b) The location of the fast-electron-density isosurface at 50% of the peak density (solid surface) and the equivalent isosurface with the magnetic field artificially suppressed (semitransparent surface).

the case with the magnetic field artificially suppressed. The expanding annulus forms because of a different mechanism than the one suggested by the simulations of Refs. 15 and 26, where an electron beam with initial half-angle divergence of 15° was used. The annular shape formed there because of excessive heating on-axis and magnetic field reversal just off-axis. The annulus did not expand radially because the magnetic field was still perfectly collimating at its outer side, resulting in simulations that did not reproduce the experimentally measured half-angle divergence of 20° (Ref. 15). In the simulations reported here, the plasma temperature maximizes in the annulus and has a minimum value on-axis in all transversal-beam cross sections except for the first ~6 μm, where the divergent beam maintains its maximum density on-axis. The formation of the annulus is not related to heating-induced field reversal as in the simulations of Refs. 15 and 26 but to partial collimation by the outside-edge field.

Comparison of the simulations with the experimental observations suggests the initial half-angle divergence of fast electrons approximately follows the ponderomotive law. It does not necessarily follow that the ponderomotive mechanism is dominant in determining the electron divergence because other mechanisms, such as the collisionless Weibel instability seen in the PIC simulations, can produce similar divergence angles.[18] More insight on this problem can be gained by applying the methodology developed in this article to the analysis of existing data obtained in other solid-target experiments (see, for instance, Ref. 20 and references therein).

In conclusion, experiments have been conducted to measure high-current, relativistic electron beams from high-intensity laser–solid interactions. High-resolution CTR imaging of the rear-side emission from metal targets reveals a structured pattern. Variations in the brightness of the emission with increasing target thickness were used to estimate a fast-electron temperature of $T_{hot} \sim 1.4$ MeV. The increase in the size of the emission region with increasing target thickness suggests a fast-electron half-angle divergence of $\theta_{1/2} \sim 16°$. Three-dimensional hybrid-PIC simulations model the details of the fast-electron transport inside the target. The spatial distribution of the fast-electron density at the rear surface reproduces the details of the CTR emission pattern by assuming an initial fast-electron half-angle divergence of $\theta_{1/2} \sim 56°$. The initial half-angle divergence is reduced in the target by the self-generated resistive magnetic field. The radially expanding annular pattern results from the partial collimation of an initially divergent fast-electron beam. Filamentation occurs in the annulus because of the resistive filamentation instability.

ACKNOWLEDGMENT

This work was supported by the U.S. Department of Energy Office of Inertial Confinement Fusion under Cooperative Agreement No. DE-FC52-08NA28302, the Office of Fusion Energy Science DE-FC02-04ER54789 (Fusion Science Center), the University of Rochester, and the New York State Energy Research and Development Authority. The support of DOE does not constitute an endorsement by DOE of the views expressed in this article.

REFERENCES

1. T. Katsouleas, Nature **444**, 688 (2006).
2. K. K. Kainz *et al*., Med. Phys. **31**, 2053 (2004).
3. W. Theobald, K. Akli, R. Clarke, J. Delettrez, R. R. Freeman, S. Glenzer, J. Green, G. Gregori, R. Heathcote, N. Izumi, J. A. King, J. A. Koch, J. Kuba, K. Lancaster, A. J. MacKinnon, M. Key, C. Mileham, J. Myatt, D. Neely, P. A. Norreys, H.-S. Park, J. Pasley, P. Patel, S. P. Regan, H. Sawada, R. Shepherd, R. Snavely, R. B. Stephens, C. Stoeckl, M. Storm, B. Zhang, and T. C. Sangster, Phys. Plasmas **13**, 043102 (2006).
4. C. A. Brau, Science **239**, 1115 (1988).
5. M. Tabak *et al*., Phys. Plasmas **1**, 1626 (1994).
6. S. C. Wilks and W. L. Kruer, IEEE J. Quantum Electron. **33**, 1954 (1997).
7. H. Popescu *et al*., Phys. Plasmas **12**, 063106 (2005).
8. M. Storm, I. A. Begishev, R. J. Brown, C. Guo, D. D. Meyerhofer, C. Mileham, J. F. Myatt, P. M. Nilson, T. C. Sangster, C. Stoeckl, W. Theobald, and J. D. Zuegel, Rev. Sci. Instrum. **79**, 10F503 (2008).
9. L. Gremillet, G. Bonnaud, and F. Amiranoff, Phys. Plasmas **9**, 941 (2002).
10. D. R. Welch *et al*., Phys. Plasmas **13**, 063105 (2006).
11. A. A. Solodov, K. S. Anderson, R. Betti, V. Gotcheva, J. F. Myatt, J. A. Delettrez, S. Skupsky, W. Theobald, and C. Stoeckl, Phys. Plasmas **16**, 056309 (2009).
12. J. Zheng *et al*., Phys. Plasmas **10**, 2994 (2003).
13. J. Myatt, W. Theobald, J. A. Delettrez, C. Stoeckl, M. Storm, T. C. Sangster, A. V. Maximov, and R. W. Short, Phys. Plasmas **14**, 056301 (2007).
14. V. Bagnoud, I. A. Begishev, M. J. Guardalben, J. Puth, and J. D. Zuegel, Opt. Lett. **30**, 1843 (2005).
15. P. A. Norreys *et al*., Plasma Phys. Control. Fusion **48**, L11 (2006).
16. S. Agostinelli *et al*., Nucl. Instrum. Methods Phys. Res. A **506**, 250 (2003).
17. B. Chrisman, Y. Sentoku, and A. J. Kemp, Phys. Plasmas **15**, 056309 (2008).
18. J. C. Adam, A. Héron, and G. Laval, Phys. Rev. Lett. **97**, 205006 (2006).
19. A. R. Bell and R. J. Kingham, Phys. Rev. Lett. **91**, 035003 (2003).
20. J. S. Green, V. M. Ovchinnikov, R. G. Evans, K. U. Akli, H. Azechi, F. N. Beg, C. Bellei, R. R. Freeman, H. Habara, R. Heathcote, M. H. Key, J. A. King, K. L. Lancaster, N. C. Lopes, T. Ma, A. J. MacKinnon, K. Markey, A. McPhee, Z. Najmudin, P. Nilson, R. Onofrei, R. Stephens, K. Takeda, K. A. Tanaka, W. Theobald, T. Tanimoto, J. Waugh, L. Van Woerkom, N. C. Woolsey, M. Zepf, J. R. Davies, and P. A. Norreys, Phys. Rev. Lett. **100**, 015003 (2008).
21. F. N. Beg *et al*., Phys. Plasmas **4**, 447 (1997).
22. P. M. Nilson, W. Theobald, J. Myatt, C. Stoeckl, M. Storm, O. V. Gotchev, J. D. Zuegel, R. Betti, D. D. Meyerhofer, and T. C. Sangster, Phys. Plasmas **15**, 056308 (2008).
23. C. I. Moore, J. P. Knauer, and D. D. Meyerhofer, Phys. Rev. Lett. **74**, 2439 (1995).
24. M. H. Key, Phys. Plasmas **14**, 055502 (2007).
25. S. I. Braginskii, in *Reviews of Plasma Physics*, edited by Acad. M. A. Leontovich (Consultants Bureau, New York, 1965), Vol. 1, p. 205.
26. J. R. Davies, J. S. Green, and P. A. Norreys, Plasma Phys. Control. Fusion **48**, 1181 (2006).